

Instabilities in downslope propagating gravity currents

Edward W. G. Skevington¹, Charlie J. Lloyd¹, A. Atoufi², and A. Doak³

¹Energy and Environment Institute, University of Hull, HU6 7RX, UK

²Department of Applied Mathematics and Theoretical Physics, Centre for Mathematical Sciences, Wilberforce Road, Cambridge CB3 0WA, UK

³University of Bath, BA2 7AY, UK

October 2023

Abstract

In this paper, the stability of a gravity current propagating down an inclined channel is explored. The gravity current is generated through a partial lock release. A local analysis of the flow about the lock is conducted using classical methodologies in two-layer shallow water theory, which is here developed to allow for drag and an angled channel. A global analysis of the flow is done by exploring the long-time forced steady state, using non-linear simulations solving the full three-dimensional Navier-Stokes equations. A steady state is forced through the inclusion of a so-called mask function. For sufficiently large slope angles, wave-like instabilities are observed on the density interface (pycnocline) of the generated gravity current. Spectral Proper-Orthogonal Decomposition of the time-series data provides evidence that instability arises via the interaction of two asymmetric vorticity waves, occurring on either side of a critical layer, akin to a spatially evolving Kelvin-Helmholtz instability. The work in this paper is exploratory in nature and motivates further investigation.

1 Introduction

Many environmental fluid flows fall under the broad category of gravity currents, where a density difference between the current and its surrounding ambient drives predominantly horizontal fluid motion (Simpson, 1997; Ungarish, 2020). Examples include the spreading of toxic gas (Rottman *et al.*, 1985), oil spillages (Hoult, 1972), cold fronts (Simpson, 1997), katabatic winds (Simpson, 1997), salinity currents (Simpson, 1982), and turbidity currents (Simpson, 1982).

To explore these currents laboratory experiments are used. One classical experiment is to separate two regions of a flume by a lock-gate, establish a density difference between the two sides using a solute, and then remove the gate generating a highly unsteady current (Simpson, 1997). The unsteadiness of such a current is often undesirable, the physics of these flows being sufficiently challenging without it, and a steady current is preferred. One method to achieve this is to use a lock gate that only partially raises, or a pair of gates with one being completely removed and the other acting as a barrier blocking the upper portion of the flow. This setup has been used to explore gravity currents colliding with obstacles (Lane-Serff *et al.*, 1995; Baines & Whitehead, 2003; Pari *et al.*, 2017) or flowing over slope breaks (Negretti *et al.*, 2017). Baines & Whitehead (2003) used this setup to simulate a current in an angled flume. To make a meaningful comparison between theory and experiments for the flow in the flume, the inflow generated by the exchange under the lock must be understood in detail, which is our aim in this work.

Previous theoretical work has explored flow under a lock using two-layer shallow water theory, often motivated by ventilation flows through a doorway or other constriction. The fundamental theory was developed by Armi (1986), Armi & Farmer (1986), and Farmer & Armi (1986), who classified solutions for steady flow. In particular they explored the special case of fully controlled flow through a constriction where small disturbances propagate away from the controlling constriction. A solution algorithm was developed by Dalziel (1991) for these flows and showed good agreement with experiments in Dalziel & Lane-Serff (1991). All the work discussed so far employed a hydrostatic pressure and neglected drag, which were first introduced into the model by Zhu & Lawrence (2000). However, their construction of fully controlled flows was incorrect, as we will discuss. Another modification to the two-layer theory that has been made is to include mixing through a varying volume flux (Laanearu & Cuthbertson, 2023), which has been applied to non rectangular channels through the approach of Laanearu & Davies (2007).

Due to the choice of application, the validation of these models has used a small lock (or a barrier on the floor) to mimic a doorway in a corridor (or oceanic sill), however the experimental setup we wish to explore has a large lock with a narrow opening, and thus we will expect a plume upstream as modelled by Nabi & Flynn (2013), using the theory of Dalziel (1991) for the exchange under the lock. They present a comparison between theory and experiments, with experiments performed in an un-angled flume, and show a good comparison in the transient dynamics, including the moving front and reflected bore.

Numerical methods have also been adopted to investigate lock-release type gravity currents (e.g. Härtel *et al.*, 2000; Gonzalez-Juez *et al.*, 2009; Ooi *et al.*, 2009; Nasr-Azadani & Meiburg, 2014; Wu & Ouyang, 2020). Typically, currents are formed through an initial condition that horizontally separates a dense fluid from a less dense fluid by an infinitesimally thin vertical boundary. At run-time, two gravity currents are produced propagating in opposite directions, with well-defined heads characterised by strong three-dimensionality and high levels of entrainment, and instabilities developing at the interface between them (of Kelvin-Helmholtz type), depending on the initial density difference and the difference between momentum and scalar (density) diffusivities. In contrast, comparatively few studies have investigated the exchange flow and resulting gravity current beneath a partially opened lock-gate (Tokuyay & Constantinescu, 2015). Despite resolving the exchange flow beneath a partially opened gate, interest has so far been focused on interactions between currents and topography rather than developing an understanding of how such an exchange flow influences the current that propagates downstream. As we shall show in this work, the exchange flow can lead to a sharp interface susceptible to wave-like instabilities dominating dynamics in the body of lock-released gravity currents.

Here, we document work started at the 2023 Summer Programme to investigate the exchange flow under a lock gate as it would be used to seed a flow in an experiment (Lane-Serff *et al.*, 1995; Baines & Whitehead, 2003; Pari *et al.*, 2017; Negretti *et al.*, 2017). We allow for the possibility that the flume is mounted at an angle, and focus on the steady flow that would be seen at intermediate times before the reflected bore returns. We do this using two approaches. Firstly, we extend the two layer shallow water model to include an angled flume and drag. We present a solution algorithm for this system and an example solution. Secondly, we present some 3D simulations of the exchange flow and resulting gravity current, demonstrating unexpected instability at the interface of the two fluids with a dependence on the slope angle. Further work will unify the two approaches such that theoretical closures can be validated and revised. In addition, the instability observed at the interface of the two fluids will be explored and quantified through further simulations of a wider parameter space and linear stability analysis.

2 Formulation

We investigate the generation and stability of a gravity current generated by flow under a partial lock-gate. A finite size tank is separated into two regions by a wall, with a gap at the bottom of the wall which is initially blocked by a movable gate. The left and right sides of the tank are filled with fluids of density ρ_1 and ρ_2 respectively, where $\rho_1 > \rho_2$. We take a Cartesian coordinate system (x, y, z) attached to the angled tank such that x is directed along the tank centre, y is the cross channel direction, and z is parallel to the vertical walls of the tank. The tank has dimensions (L_x, L_y, L_z) , and is tilted such that the coordinate system and channel are at an angle θ downhill so that gravity is $(g \sin \theta, 0, -g \cos \theta)$. The movable gate has length L_g . Upon release of the lock-gate, a confined buoyant plume is realised in the dense fluid region, while a gravity current propagates along the bottom of the tank in the lower-density region. Figure 1 shows the flow configuration.

For numerical simulations, we choose dimensions of the tank such that the two fluids are separated by a wall which has an opening of height $L_g = 1$. The domain size is $L_x = 25$ in the streamwise direction, $L_z = 10$ in the vertical direction, and $L_y = \pi$ in the spanwise y direction. The domain is partitioned by the gate into a region of length 5 upstream and 20 downstream, a choice motivated by typical lock-release type laboratory experiments.

Denoting the velocity vector $\mathbf{u} = (u, v, w)$, the pressure p , and the unit-normal to the boundaries $\hat{\mathbf{n}}$, we enforce no-slip ($\mathbf{u} = 0$) and insulated walls ($\nabla \rho \cdot \hat{\mathbf{n}} = 0$) on the x and z normal boundaries, and periodic boundary conditions are applied in the spanwise (y) direction. These boundary conditions, along with the Boussinesq Navier-Stokes equations (defined in Section 4), form a closed system for the unknowns $\{\mathbf{u}, p, \rho\}$. Before describing the numerical method used to solve this system and presenting the results, we first explore a shallow water model which attempts to capture the local flow behaviour about the gate.

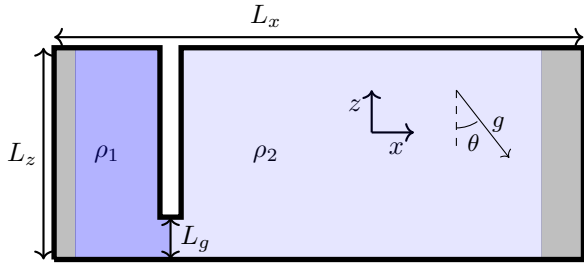


Figure 1: Flow configuration. The flow is initialised with a partial lock release, and a region of higher density ρ_1 forms a gravity current as it enters the region of lower density ρ_2 . The forcing regions (discussed in Section 4) are marked in grey.

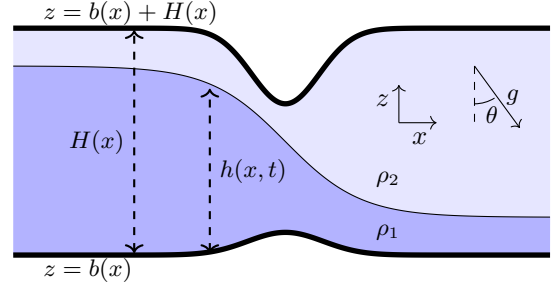


Figure 2: Configuration of the two-layer shallow-water theory. It provides a toy-model for the local behaviour of the flow about the lock release under the gate. The bottom topography $z = b(x)$ is included in the figure but is taken to be zero in the case of flow under a gate.

3 Shallow-water theory of lock exchange

We here extend the classical hydraulic theory of lock exchange, largely summarised in Dalziel (1991), to account for flow on slopes with drag or other forcing. The reduced order model derived here decreases the complexity of the equations, allowing analytical insights into gravity current properties. The model makes many assumptions about the flow, as described below, but nonetheless provides insight into the behaviour of the flow under the gate. We include bathymetry in the derivation, in part so that the model can more generally be applied to gravity current interactions with bathymetry and bed slope, but primarily because it allows for a useful interpretation of the effect of drag.

The upper level of the channel is denoted by $z = b(x) + H(x)$, where $b(x)$ is the bed elevation and $H(x)$ the channel depth. For the problem we consider here $b(x) = 0$ (but we include the general case), and $H(x)$ takes a constant value of H_0 except around the lock. The flow configuration is shown in Figure 2. The hydraulic theory employs a two layer shallow water model, where there is a sharp jump between the two layers at some elevation $h(x, t)$ (neglecting all variation and movement in the y direction). The region $0 < z - b < h$ is termed layer 1 and $h < z - b < H$ layer 2, and we use subscripts to distinguish between the layers. In each layer the density ρ_i is treated as constant, the pressure hydrostatic, and the x -component of velocity $u_i(x, t)$ independent of z . We assume that the flow is Boussinesq, that is $0 < \rho_1 - \rho_2 \ll \rho_r$ where $\rho_r = \frac{1}{2}(\rho_1 + \rho_2)$ is the reference density. The time-dependent governing equations are then

$$\frac{\partial h_i}{\partial t} + \frac{\partial}{\partial x}(h_i u_i) = 0, \quad (1a)$$

$$\frac{\partial}{\partial t}(h_i u_i) + \frac{\partial}{\partial x}(h_i u_i^2) + \int_{z_{i-1}}^{z_i} \frac{1}{\rho_r} \frac{\partial p_i}{\partial x} dz = \frac{\rho_i - \rho_r}{\rho_r} g h_i \sin \theta + h_i F_i \quad \text{for } i \in \{1, 2\}. \quad (1b)$$

In these equations, p is the pressure relative to the hydrostatic pressure of the reference density (z dependent and continuous between layers), $z_0 = b$, $z_1 = b + h$ and $z_2 = b + H$ are the interface elevations, $h_1 = h$ and $h_2 = H - h$ are the layer thicknesses, and F_i capture additional forces such as shear forces acting across interfaces. The hydrostatic pressure can be expressed as

$$\begin{aligned} p &= p_2 = p_H + (\rho_2 - \rho_r)g(H + b - z) \cos \theta & \text{for } h < z - b < H, \\ p &= p_1 = p_H + (\rho_2 - \rho_r)g(H - h) \cos \theta + (\rho_1 - \rho_r)g(h + b - z) \cos \theta & \text{for } 0 < z - b < h, \end{aligned} \quad (2)$$

where p_H is the pressure at $z = b + H$. Using that in each layer $\partial p_i / \partial x$ is independent of z , along with conservation of volume (1a), conservation of momentum (1b) can be rewritten as

$$\frac{\partial u_i}{\partial t} + \frac{\partial G_i}{\partial x} = F_i \quad \text{where} \quad G_i = \frac{1}{2} u_i^2 + \frac{p_i}{\rho_r} + \frac{\rho_i - \rho_r}{\rho_r} g(z \cos \theta - x \sin \theta) \quad (3)$$

is the Bernoulli potential of the streamline. Consequently, steady shallow water flow may be understood as enforcing conservation of energy up to any work done by the forces F_i . To eliminate the unknown pressure p_H from the system we take the difference between the two layers to obtain

$$\frac{\partial}{\partial t}(u_1 - u_2) + \frac{\partial \Delta G}{\partial x} = \Delta F \quad \text{where} \quad \Delta G = G_1 - G_2 = \frac{1}{2}(u_1^2 - u_2^2) + g'((h + b) \cos \theta - x \sin \theta), \quad (4)$$

$\Delta F = F_1 - F_2$, and $g' = g(\rho_1 - \rho_2)/\rho_r$. For the examination of steady states ($\partial/\partial t = 0$), the equations (1a) and (4) can be written as

$$\frac{dq_1}{dx} = 0, \quad \frac{dq_2}{dx} = 0, \quad \frac{dE}{dx} = 0, \quad (5a)$$

$$\text{where } q_i = u_i h_i, \quad E = \mathcal{E} + g' \mathcal{B} \cos \theta, \quad (5b)$$

$$\mathcal{E} = \frac{1}{2} \left(\frac{q_1^2}{h^2} - \frac{q_2^2}{(H-h)^2} \right) + g' h \cos \theta, \quad \mathcal{B} = b - x \tan \theta - \frac{1}{g' \cos \theta} \int_{x_0}^x \Delta F dx. \quad (5c)$$

Here, q_1 and q_2 are the volume flux (per unit y) in the lower and upper layer respectively, and E is the total energy difference between streamline energy (per unit mass) in the two layers modified by the work done by the force difference ΔF . For the purpose of later analysis we split this energy into two components: \mathcal{E} is termed the partial energy difference and is the difference between the kinetic energy and pressure generated by flow depth, which captures the way that the energy difference depends on h (except the effects of ΔF); $g' \mathcal{B} \cos \theta$ contains the pressure difference generated by variation in bed elevation, work done by the component of gravity in the x direction, and the force difference ΔF . The purpose of splitting in this way is to obtain a system as close as possible to the system without bed elevation, downslope gravity or additional forces, for which $E = \mathcal{E}$, and incorporate all of these effects in an effective bed elevation \mathcal{B} , demonstrating that the inclusion of slope and drag does not fundamentally change the nature of the solutions. However, unlike b , \mathcal{B} is not a known function of x but something to be determined as a part of the solution, because ΔF is (in general) dependent on h_i and q_i (of course if ΔF is a function of x alone then \mathcal{B} is a known function). This will complicate finding desired solutions to the system beyond what has been explored previously (Dalziel, 1991).

Introducing some notation that will be required in the solution development, (5a) implies that $q_1 = \hat{q}$, $q_2 = \hat{Q} - \hat{q}$, and $E = \hat{E}$ where \hat{q} , \hat{Q} , and \hat{E} are constant values. Note that \hat{Q} is the net combined volume flux in the two layers, and is a parameter to set when finding a solution. Since we are concerned with local behaviour in a confined exchange flow, we will always choose $\hat{Q} = 0$. The total depth of the channel $H(x)$, bed elevation $b(x)$, reduced gravity g' , slope angle θ , and net force $\Delta F(x, h_1, h_2, q_1, q_2)$ will be considered as known going forward. We stress that \hat{q} and \hat{E} are not known a priori and must be recovered as part of the solution. These values arise as constants of integration and are the values we seek (along with $h(x)$) by imposing certain criteria. In principle, the same is true for \hat{Q} , but the criterion of vanishing net volume flux sets it to zero without additional work, while further criteria are required for \hat{q} and \hat{E} . We will first discuss some required properties of the system, in particular the properties of the functions E and \mathcal{E} defined in (5b) and (5c) respectively. From these properties we will establish the criteria for the solution, and then use these properties and criteria to develop a solution method.

3.1 Properties of the system

Suppose that at some x we have known values of H , q_1 , q_2 , E , and \mathcal{B} from which we can calculate \mathcal{E} . Deducing h from these values is not straightforward as there are often multiple values of h which yield the given value of \mathcal{E} , see Figure 3. Given $\mathcal{E} \rightarrow \infty$ as $h \rightarrow 0$ and $\mathcal{E} \rightarrow -\infty$ as $h \rightarrow H$, how many solution branches exist depends on the inflection point at which $\partial^2 \mathcal{E} / \partial h^2 = 0$, located at

$$h_I = H \frac{|q_1|^{1/2}}{|q_1|^{1/2} + |q_2|^{1/2}}, \quad \text{that is} \quad h_I = \frac{H}{2} \quad \text{when } |q_2| = |q_1|. \quad (6)$$

If, at the inflection point, $\partial \mathcal{E} / \partial h < 0$ then \mathcal{E} is monotonically decreasing. Conversely if $\partial \mathcal{E} / \partial h > 0$ at the inflection point then two extrema appear, this condition is equivalent to

$$\frac{|q_1|^{1/2} + |q_2|^{1/2}}{(g' H^3 \cos \theta)^{1/4}} \leq 1, \quad \text{that is} \quad q_1^2 \leq \frac{g' H^3 \cos \theta}{2^4} \quad \text{when } |q_2| = |q_1|. \quad (7)$$

These extrema are of key importance, and going forward we will assume that they are present. Flows located at one of these extrema are termed critical flow and satisfy $\partial \mathcal{E} / \partial h = 0$, equivalent to $Fr = 1$ where

$$Fr^2 = \frac{q_1^2}{g' h^3 \cos \theta} + \frac{q_2^2}{g' (H-h)^3 \cos \theta}, \quad \frac{\partial \mathcal{E}}{\partial h} = (1 - Fr^2) g' \cos \theta. \quad (8)$$

We denote the two values of h ($0 < h < H$) which give critical flow by $h_- \leq h_+$ ($h_- = h_+$ precisely when (7) is equality). Note that $Fr < 1$ on $h_- < h < h_+$ and $Fr > 1$ for $h < h_-$ or $h_+ < h$.

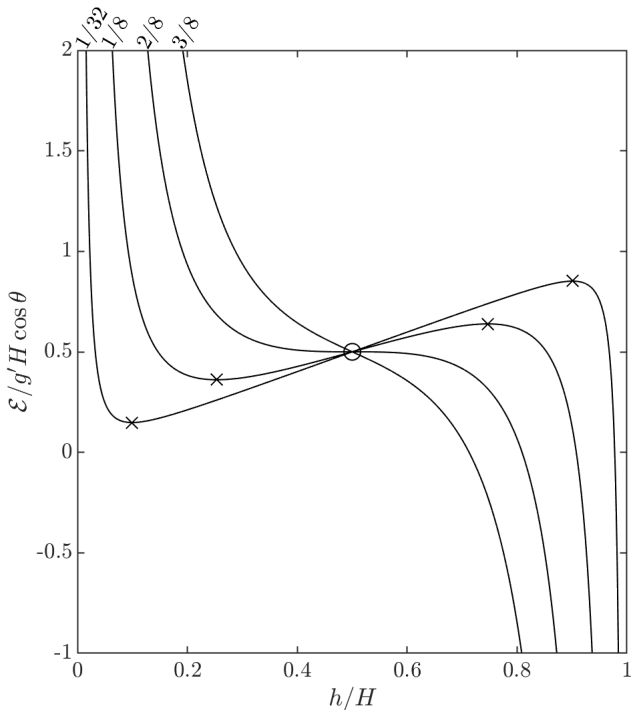


Figure 3: The energy \mathcal{E} as a function of h , each rendered dimensionless. The different curves are for different $q_1 = -q_2$ ($\hat{Q} = 0$), the values of $q_1/\sqrt{g'H^3 \cos \theta}$ are stated at the top left. The inflection point is labelled with a circle, and the critical points with crosses where the depth and energy are (h_-, \mathcal{E}_-) or (h_+, \mathcal{E}_+) .

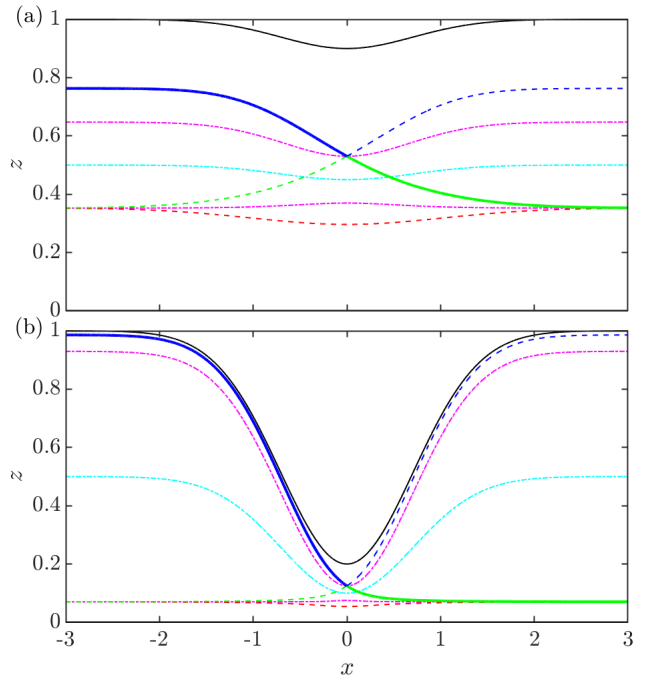


Figure 4: A side view of the flow under a lock, the bed b and lock $H + b$ potted as black lines. Here the driving force balances the drag and there is no net flow $\hat{Q} = 0$. The deep supercritical solution is shown in blue, the subcritical in green, and the shallow supercritical solution in red. The physical solution transitions from deep supercritical to subcritical along the solid lines, the unphysical solutions shown in dashed. We also show the critical depths h_{\pm} in magenta dash-dot and the inflection depth h_I in cyan dash-dot. In (a) $H_{\text{lock}} = 0.5$, in (b) $H_{\text{lock}} = 0.2$.

Low amplitude, long wavelength disturbances to the system away from steady state generate two waves with speeds $\lambda_L < \lambda_R$, and Dalziel (1991) observed that the Froude number Fr could be written as

$$Fr^2 = 1 + \frac{h_1 + h_2}{g'h_1 h_2} \lambda_L \lambda_R. \quad (9)$$

When $h_- < h < h_+$ we have that $Fr < 1$, this flow is termed subcritical and $\lambda_L < 0 < \lambda_R$, the disturbances propagate in both directions. Conversely, when $h < h_-$ or $h_+ < h$ we have $Fr > 1$ and λ_L, λ_R are of the same sign. A careful analysis (Dalziel, 1991) reveals their direction: when $h < h_-$ then the flow is shallow and supercritical, the waves swept in the direction of flow of the lower layer, while those satisfying $h_+ < h$ are deep and supercritical, waves swept in the direction of the flow of the upper layer. We will refer to flows where $h = h_-$ and $h = h_+$ as shallow and deep critical respectively.

The partial energy difference \mathcal{E} evaluated at the critical depths we denote by \mathcal{E}_{\pm} , evaluated at h_{\pm} respectively, from which we can calculate equivalent values of the full energy difference $E_{\pm} = \mathcal{E}_{\pm} + g'B \cos \theta$. Given a value of \mathcal{E} , we can see from Figure 3 which types of solution are possible. For a shallow supercritical flow ($h < h_-$) or subcritical flow ($h_- < h < h_+$) to be possible at some point x we require that $\mathcal{E}_- \leq \mathcal{E}$, which is equivalent to $E_- \leq \hat{E}$. We next consider variation in x , remembering that \hat{E} is constant in x . For the flow to continuously transition from one of these flow regimes to the other (that is transition from one branch to the other) we must have that E_- increases up to a critical point at which $E_- = \hat{E}$ after which it decreases again. Consequently, at the critical point, $E_-(x)$ is a local maximum so that $dE_-/dx = 0$. Similarly, to have either a deep supercritical flow or subcritical flow we require that $E_+ \geq \hat{E}$, and to transition from one solution branch to the other there must be a critical point at which $E_+ = \hat{E}$, and $E_+(x)$ is a local minimum so that $dE_+/dx = 0$. (These conditions can be strengthened by additionally enforcing $d^2E_-/dx^2 \leq 0$ and $d^2E_+/dx^2 \geq 0$, which we leave to future work.)

For flow under a lock gate, we expect the flow at $x \rightarrow -\infty$ to be deep (super)critical, while the flow at $x \rightarrow \infty$ is shallow (super)critical; this is the additional criteria we use to find \hat{q} and \hat{E} . Such flow is termed fully controlled and has two critical points, or in the edge case a single critical point at which $h = h_- = h_+ = h_I$. We denote the locations of the critical points by $x_+ < x_-$, with $h = h_+$ at $x = x_+$ and $h = h_-$ at $x = x_-$. Consequently, the values of the constants \hat{E} , \hat{q} are determined by identifying the locations of the critical points x_{\pm} which can be connected by flow of constant flux and total energy difference. The most straightforward algorithm is to directly solve for $(x_+, x_-, \hat{q}, \hat{E})$ under the conditions that $E_-(x_-, \hat{q}) = \hat{E}$ and $E_+(x_+, \hat{q}) = \hat{E}$ and that a subcritical solution exists on the spatial interval $x_+ < x < x_-$, see Dalziel (1991) for details. However, the algorithm will almost always reach a situation where the subcritical solution branch does not exist over the spatial interval, meaning that E_{\pm} cannot be calculated as these are dependent on \mathcal{B} which depends non-locally on the solution through an integral. Conversely the conditions $dE_-/dx = 0$ and $dE_+/dx = 0$ are local because $d\mathcal{B}/dx$ is local. Specifically

$$\frac{d\mathcal{B}}{dx} = \frac{db}{dx} - \tan \theta - \frac{\Delta F}{g' \cos \theta} \quad (10)$$

so that

$$\frac{dE_{\pm}}{dx} = \frac{q_2^2}{(H - h_{\pm})^3} \frac{dH}{dx} + g' \cos \theta \frac{db}{dx} - g' \sin \theta - \Delta F(h_{\pm}). \quad (11)$$

There is no term proportional to dh_{\pm}/dx because $\partial\mathcal{E}/\partial h = 0$ at $h = h_{\pm}$. Consequently, without needing to know \mathcal{B} , for any given location x we can find what fluxes q_1 can yield critical flow (for some E) by solving (11) with $q_2 = \hat{Q} - q_1$. This allows candidate sets (x_-, x_+, \hat{q}) to be established before seeking the value of \hat{E} . We briefly contrast condition (11) with that used by Zhu & Lawrence (2000), who (translating to our notation) stated that the effect of drag was to move the critical points to locations where $g' \cos \theta \cdot db/dx = \Delta F$. We see that this is only true when $g' \sin \theta = 0$ and $dH/dx = 0$, and while the former was true in their setup the latter was not.

Before giving the general solution method for fully controlled flow, we give a simple example, taking $\hat{Q} = 0$, $b = 0$, $\Delta F = -g' \sin \theta$, and $H = 1 + (H_{\text{lock}} - 1) \exp(-x^2)$, choosing units so that $g' \cos \theta = 1$. At the critical points we require $dE_{\pm}/dx = 0$ which implies that $dH/dx = 0$. Consequently, the critical points are at $-\infty$, 0 , or ∞ . The final step is to choose a pair of points $x_+ < x_-$ and solve $E_+(x_+, \hat{q}) = E_-(x_-, \hat{q})$ as a function of $\hat{q} = q_1(x_+) = q_1(x_-)$, which yields the constant values of \hat{E} and \hat{q} . This final step is the only time when the value of \mathcal{B} is required, and constitutes finding the root of a scalar single variable function.

Solutions are plotted in Figure 4, which have $x_+ = 0$ and $x_- \rightarrow \infty$. This allows for a transition from deep supercritical flow on $x < 0$ to subcritical flow on $x > 0$ tending to shallow critical flow at $x \rightarrow \infty$. This is the solution we expect to manifest physically, and is shown as solid lines, while the other solution branches will not be seen and are plotted in dashed lines. We also show the critical and inflection depths in dot dashed lines, which do not satisfy the governing equations but rather are part of the solution construction.

3.2 The solution algorithm

To illustrate the solution algorithm, we consider the problem $\hat{Q} = 0$, $b = 0$, $h\Delta F = -C_D u_1^2 = -C_D q_1^2/h^2$, and $H = 1 + \frac{1}{2} \exp(-x^2)$, choosing units so that $g' \cos \theta = 1$. We treat the drag as simply the drag between the lower layer and the bed, which will be approximately true for the physically important region downstream of the lock. We require that the solution tend to some limit on $x \rightarrow \infty$, and consequently there must be a constant valued solution for H constant. A constant valued solution is straightforward to construct from $d\mathcal{B}/dx = 0$ which gives $\Delta F = -g' \sin \theta$, that is

$$h = \left(\frac{C_D \hat{q}^2}{g' \sin \theta} \right)^{1/3}. \quad (12)$$

At finite x , in particular around the lock-gate, the solution will not take on this constant value. Consequently, for the steady state to exist, the solution must tend towards the constant solution as x increases. To identify whether this is the case, we perturb it as

$$h(x) = (1 + \epsilon \tilde{h}(x)) \left(\frac{C_D \hat{q}^2}{g' \sin \theta} \right)^{1/3} \quad (13)$$

and substitute into (5c) to obtain at leading order for $0 < \epsilon \ll 1$

$$\frac{d\tilde{h}}{dx} = \frac{3 \tan \theta}{1 - Fr^2} \tilde{h}, \quad (14)$$

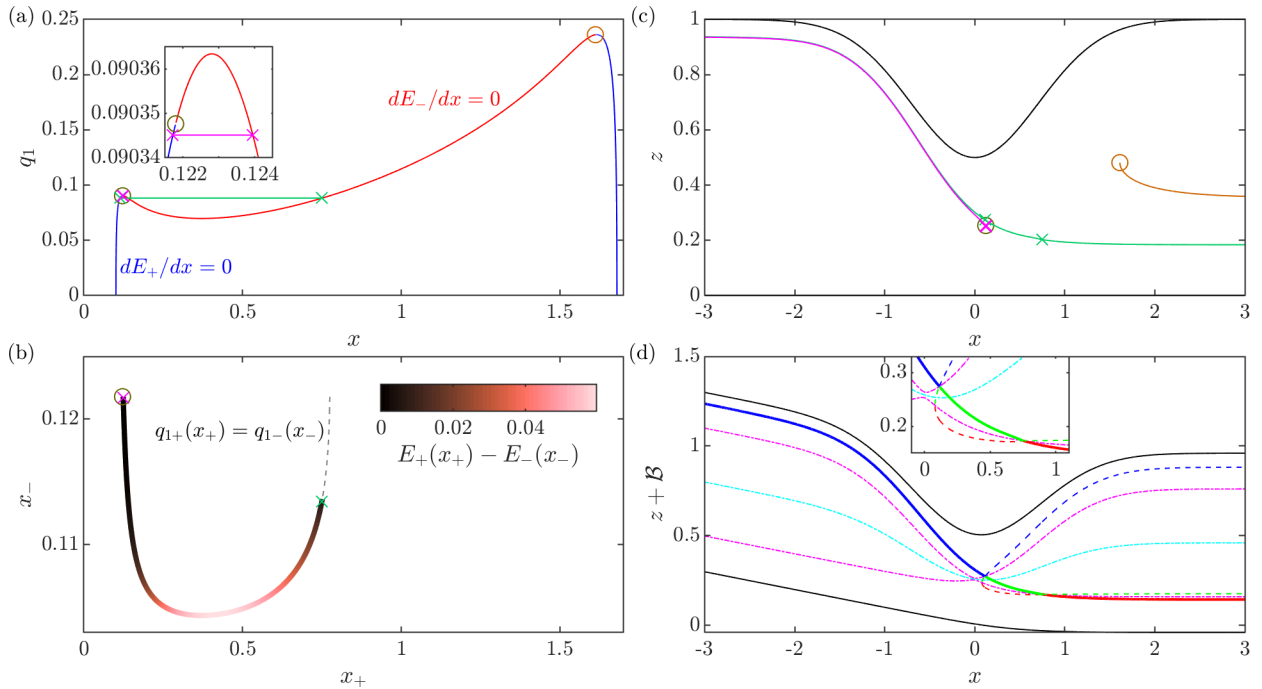


Figure 5: Illustration of the solution algorithm for forced shallow water flow on a slope. (a) The solutions to $dE_{\pm}/dx = 0$, with the solutions to $q_{1+}(x_+) = q_{1-}(x_-)$, $E_+(x_+) = E_-(x_-)$ marked with crosses if $x_+ < x_-$ and circles if $x_+ = x_-$. (b) The solution to $q_{1+}(x_+) = q_{1-}(x_-)$, coloured by the difference $E_+(x_+) - E_-(x_-)$; where the difference cannot be calculated because there is no valid depth on the subcritical solution branch then the curve is marked with a grey dashed line. The solutions to $E_+(x_+) = E_-(x_-)$ are marked with crosses and circles as previously. (c) The solutions plotted as functions of x , only one exists for all x which is the unique solution to this problem. (d) The solution plotted as though B were the bed elevation using the same line styles as in Figure 4.

where Fr is evaluated at $\epsilon = 0$. Consequently, for $\tilde{h} \rightarrow 0$ as $x \rightarrow \infty$, we require that the flow is supercritical $Fr^2 > 1$. Thus, we are looking for a fully controlled solution which does not just tend to criticality at large x , but rather crosses through criticality at finite x to shallow supercritical flow.

Our goal, then, is to construct a fully controlled solution, which was discussed in Section 3.1. We will need to find a point x_+ at which the flow is deep critical, and another at which x_- is shallow critical at the same flux \hat{q} , remembering that $x_+ < x_-$, and then connect these by a solution of constant energy \hat{E} , the result of the algorithm being the full set of values $(x_+, x_-, \hat{q}, \hat{E})$ from which $h(x)$ can be constructed. This algorithm assumes that $H(x)$, $b(x)$, g' , θ , $\Delta F(x, h_1, h_2, q_1, q_2)$ and \hat{Q} are known. The algorithm is illustrated in Figure 5 where we take $\tan \theta = 0.1$ and $C_D = 0.08$. We will state the operation to perform in italic text, and give some details in roman text.

1. *For each x , solve the equation $dE_-/dx = 0$ for q_1 producing a function $q_{1-}(x)$, and similarly solve $dE_+/dx = 0$ for q_1 producing a function $q_{1+}(x)$, in both cases taking $q_2 = \hat{Q} - q_1$ (11). See Figure 5(a).* In practice an array of values of x will be used that is sufficiently dense for subsequent steps to use an interpolation of the solution to generate $q_{1\pm}(x)$. Not every x will have a solution, and root-finding will be required to find values of x where the solutions come into existence. The resulting solution curves show the value of the flux q_1 required for shallow critical flow ($q_{1-}(x)$) or deep critical flow ($q_{1+}(x)$) at each x . A particular value of E will be required also, not calculated here.
2. *Identify all triplets (x_+, x_-, \hat{q}) , $x_+ \leq x_-$, satisfying $q_{1+}(x_+) = q_{1-}(x_-) = \hat{q}$.* See Figure 5(b). Practically, we construct a discrete representation of curves through (x_+, x_-) space which satisfy $q_{1+}(x_+) = q_{1-}(x_-)$, and then set \hat{q} to this value of flux. For each triplet (x_+, x_-, \hat{q}) on this curve, there is some function $B(x)$ for which there is a fully controlled flow that is critical at these two points with the given flux at some \hat{E} . Consequently, we have here constructed all solutions with constant flux \hat{q} satisfying the local properties of criticality, but not the non-local property of constant \hat{E} .
3. *Identify the triplets (x_+, x_-, \hat{q}) satisfying $E(x_+, \hat{q}) - E(x_-, \hat{q}) = 0$ through root finding. This gives the value of \hat{E} for the solution through $\hat{E} = E_+(x_+, \hat{q}) = E_-(x_-, \hat{q})$ yielding $(x_+, x_-, \hat{q}, \hat{E})$.* See Figure 5(b).

To compute the value $E_+(x_+, \hat{q}) - E_-(x_-, \hat{q})$ we need to know the difference in effective bed elevation $\mathcal{B}(x_+) - \mathcal{B}(x_-)$. This is calculated by solving the differential equation (10) over the interval $x_+ < x < x_-$. Starting at $x = x_+$, $h = h_+$, $\mathcal{B} = 0$, $\hat{E} = E_+(x_+, \hat{q})$, we integrate (10) over the interval taking h on the subcritical branch to obtain $\mathcal{B}(x_-)$. This integration process is the most expensive part of the solution process, which is why we save it for last. Sometimes, the integration will reach a point at which there is no subcritical value of h , in which case the integration is abandoned.

While this solution method gives tuples for the form $(x_+, x_-, \hat{q}, \hat{E})$, and for each tuple there is a solution $h(x)$ in the interval $x_+ \leq x \leq x_-$, there is no guarantee the solution extends outside of this interval. In Figure 5(c) we attempt to integrate the solutions outside of this interval. For one of the solutions, the integration is successful, producing a solution for all x . For the other with $x_+ \leq x_-$ the shallow supercritical solution branch ceases to have a solution on $x > x_-$ invalidating the solution. We also plot the cases where $x_+ = x_-$ and the solution can, in principle, transition directly from deep supercritical to shallow supercritical through the inflection point; the integration fails in both cases. Consequently, we arrive at the unique fully controlled flow for this setup.

For illustrative purposes, we plot the solution in Figure 5(d) treating the found \mathcal{B} as the bed elevation. This shows that the solutions to the present system are of the same type, if more general, than those discussed by Armi (1986) and Dalziel (1991).

4 Simulations

To arrive at the shallow water model of Section 3 several key assumptions are made about the flow; namely that the pycnocline is infinitesimally thin, the fluids immiscible and inviscid, and the resulting flow is (to leading order) hydrostatic with velocity independent of z in each layer. These assumptions are restrictive, and so to supplement this theory we simulate a lock-gate flow and the resulting gravity current using 3D Large-Eddy-Simulations (LES). To construct a pseudo-steady flow we implement artificial forcing, allowing a study of the key features of lock-release gravity currents and their dependence on the slope angle.

4.1 Methodology

We directly solve the dimensionless momentum and continuity equations with a scalar transport equation for density:

$$\frac{D\mathbf{u}}{Dt} = -\nabla p + \frac{1}{Re} \nabla^2 \mathbf{u} - \rho \hat{\mathbf{g}} + \mathbf{F}_u, \quad (15)$$

$$\nabla \cdot \mathbf{u} = 0, \quad (16)$$

$$\frac{D\rho}{Dt} = \frac{1}{RePr} \nabla^2 \rho + F_\rho. \quad (17)$$

The flow is made dimensionless by the buoyancy velocity, $u_b = \sqrt{g' L_g}$, where $g' = (\rho_1 - \rho_2)g/\rho_2$ is the reduced gravitational acceleration and L_g is the opening height beneath the lock gate. Note that in contrast to the shallow-water formulation, generalised to seek solutions for arbitrary lock-gate topography, here we seek numerical solutions for the exchange flow underneath a rectangular lock-gate opening with dimensions $L_g = 1$ in height and 0.2 in width. The dimensionless density field is equal to $\rho = \frac{\hat{\rho} - \rho_2}{\rho_1 - \rho_2}$ where $\hat{\rho}$ is the dimensional density, ρ_1 is the density of the current, and ρ_2 is the density of the ambient, such that $\rho = 0$ when $\hat{\rho} = \rho_2$ and $\rho = 1$ when $\hat{\rho} = \rho_1$. The gravity vector $\hat{\mathbf{g}} = (\sin \theta, 0, -\cos \theta)$ has magnitude unity and acts at some angle θ from the vertical direction. For $\theta > 0$, gravity acts as if the domain sketched in Figure 1 were tilted clockwise. The Reynolds number is defined as $Re = u_b L_g / \nu = 1000$, and the Prandtl number is $Pr = \kappa / \nu = 1$. This work investigates solutions using two slope angles: $\theta = 0$ and $\theta = 10$ degrees, units henceforth omitted.

The forcing terms \mathbf{F}_u and F_ρ are used to restore the velocity and density fields at the extremes of the streamwise domain over some timescale τ_f :

$$\mathbf{F}_u = -\frac{\mathbf{u}}{\tau_f} \cdot f(x), \quad F_\rho = -\frac{\rho - \rho_0(x)}{\tau_f} \cdot f(x) \quad (18)$$

where

$$\rho_0(x) = \begin{cases} 1, & \text{for } x < 0, \\ 0, & \text{for } x \geq 0. \end{cases} \quad (19)$$

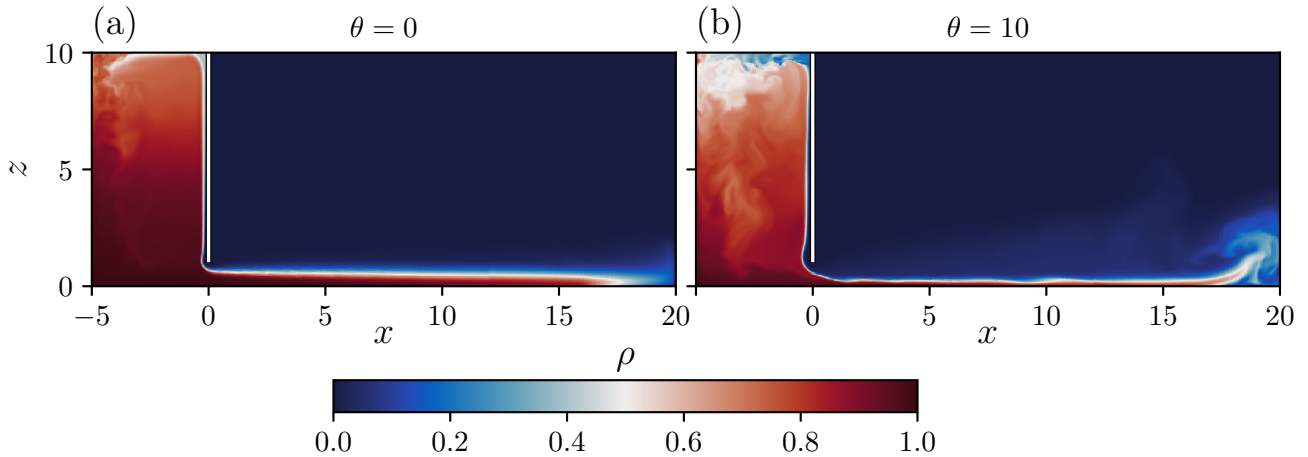


Figure 6: Instantaneous density fields on a y normal slice at $y = \pi/2$ for $\theta = 0$ (a) and $\theta = 10$ (b).

and the mask function $f(x)$ is given by

$$f(x) = 1 - 0.5 \tanh(s(x + 4)) + 0.5 \tanh(s(x - 16)), \quad (20)$$

where s controls the width of the transitions from the fully unforced region where $f \simeq 0$ to the fully forced region where $f \simeq 1$. The origins of the two \tanh functions are set to $x = -4$ and $x = 16$, such that 20% of respective fluid reservoirs are relaxed towards $\mathbf{u} = 0$ and $\rho = \rho_0$ (see Figure 1). The timescale τ_f controls the rates at which the fields are relaxed. The cases presented here fix $\tau_f = 10$ and $s = 10$. Through this forcing strategy, we simulate a quasi steady-state system indicative of one with a spatial domain much larger. Such forcing enables the exchange flow to be analysed using techniques suitable for steady-state analysis, such as spectral POD. Further details of this forcing, and examples of its application to stably stratified shear flows, can be found in Zhu et al. (2023) where a similar forcing strategy has been employed to generate arbitrarily long simulations of exchange flow in stratified inclined ducts.

The domain is discretised into $N_{xz} \times N_y = 4444 \times 10$ body-fitted spectral elements, such that the gate boundaries are explicitly resolved. Elements are clustered near the walls and at $z = H$, such that more elements are present in the lower regions of the domain where the gravity current propagates. Each element is further discretised by 8^3 Gauss-Lobatto-Legendre (GLL) nodes, and solved using NEK5000 (2019). Equations are integrated in time using third-order backward differencing with a timestep of 10^{-3} , and nonlinear terms are dealiased using the $3/2$ rule.

Subgrid scales are accounted for using modal based explicit filtering, equivalent to deconvolution LES or hyper-viscosity (Fischer et al., 2001; Chatterjee & Peet, 2018). This filtering technique has been adopted and validated for stratified and wall-bounded turbulent flows (Lai et al., 2019; Jin et al., 2021; Lloyd et al., 2022). Note, however, that the main influence of sub-grid scale filtering occurs in the wall-attached plume of the ambient fluid into the denser fluid reservoir; the gravity current and the interface beneath the lock-gate, are well resolved.

Simulations are performed by initialising the flow with ρ_0 and letting the system evolve to a pseudo-steady state. Once reached, time-averaging is performed to obtain mean flow fields, and instantaneous data are sampled on a spanwise-normal slice to obtain spatio-temporal coherence. Data are sampled on a uniform $x - z$ grid of resolution 500×250 grid points every 100 timesteps.

4.2 Results

The instantaneous flow after a quasi-steady state has been reached is visualised by the density field in Figure 6. The lock gate sets up an exchange flow with a dense current moving rightwards beneath the leftwards-moving ambient flow. The ambient flow subsequently generates a fast vertically moving buoyant plume as it passes the gate opening. As it rises it impinges on the upper boundary and generates strongly turbulent flow, setting up a recirculating flow cell which diffuses the density field in the dense fluid reservoir (Figure 6). This upper region of the dense reservoir (ceiling) is the most active in the domain. The influence of the forcing terms is clear in Figure 6, particularly for the $\theta = 0$ gravity current as it tends towards $x = 20$.

Temporally and spanwise-averaged velocity magnitude and density are presented in Figures 7 and 8, where variables have been decomposed into their time and planar averaged components, represented with an overbar,

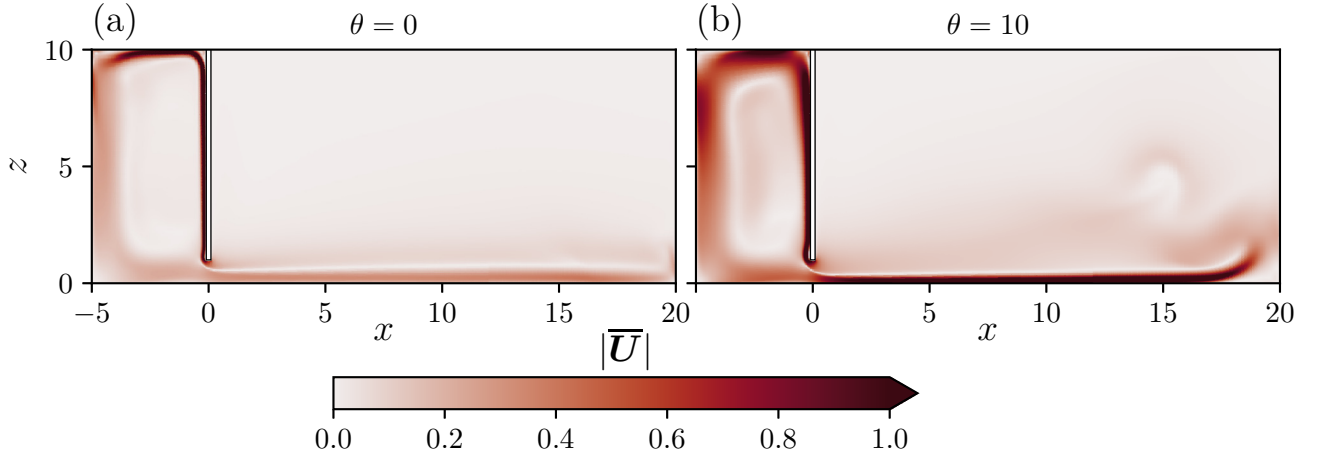


Figure 7: Temporally and spanwise-averaged velocity magnitude for $\theta = 0$ (a) and $\theta = 10$ (b).

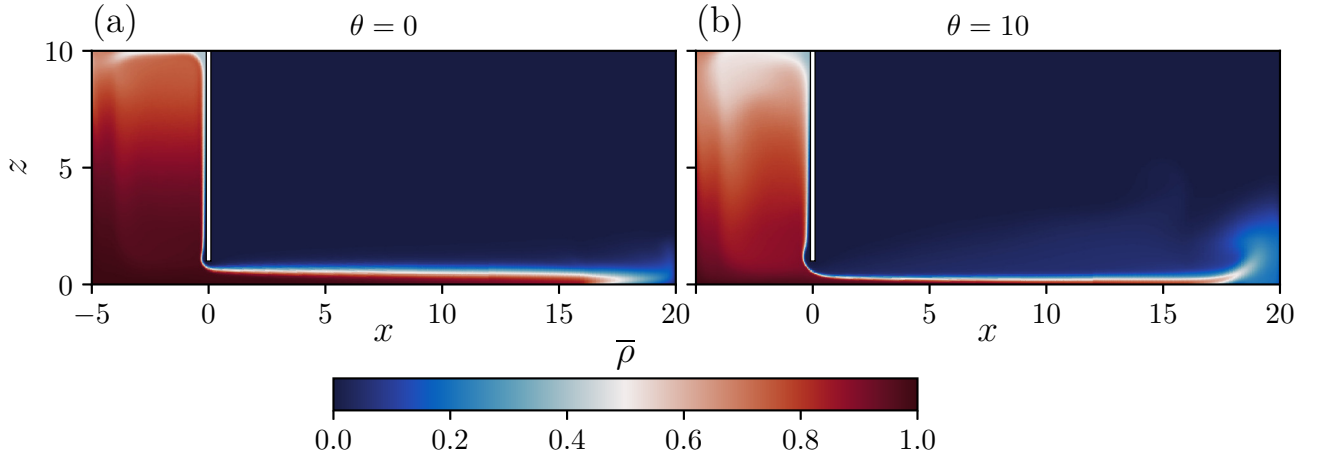


Figure 8: Temporally and spanwise-averaged density fields for $\theta = 0$ (a) and $\theta = 10$ (b).

and their fluctuating components, represented by primes: $\mathbf{u} = \bar{\mathbf{U}} + \mathbf{u}'$, $\rho = \bar{\rho} + \rho'$, where $\bar{\mathbf{U}} = (\bar{U}, \bar{V}, \bar{W})$ and $\mathbf{u}' = (u', v', w')$ in (x, y, z) . The mean flow fields clearly demonstrate the strong influence of θ on the current; at $\theta = 10$ we observe a thinner, faster current when compared to the zero slope case. The mean velocity magnitude field of Figure 7 also highlights the recirculating flow cell in the dense fluid reservoir, generated from the impinging ambient plume on the upper wall and the flux of dense fluid through the gate. This recirculating fluid has its density restored to ρ_1 as it moves downwards at the left boundary, which subsequently feeds into the density current through the gate. Likewise, as the dense gravity current approaches $x = 20$ its density field is relaxed towards ρ_2 and its velocity field is relaxed towards zero, subsequently generating a very weak upward movement of fluid, compared to the velocity magnitudes in the dense fluid reservoir. This ensures the ambient fluid density is restored such that a steady current can be sustained. Note, however, that the effective Reynolds number is reduced as the simulation reaches this steady state due to the turbulent diffusion of the density field, particularly in the dense fluid reservoir. The extent of this reduction in density is controlled by the balance between the forcing timescale, τ_f , and the rate at which the density field is mixed.

Quantitative differences between the two flows are more clear in the profiles of Figure 9 which sample the mean flow data of Figures 7 and 8 at $x = 5$. The narrower current of the $\theta = 10$ case is complemented with a thinner interface thickness, approximated by z values corresponding to 90% bounds on $\bar{\rho}$. We subsequently observe higher density gradients, and substantially higher velocity gradients, for $\theta = 10$ when compared to $\theta = 0$.

By increasing the slope angle we also observe a transition in the stability of the gravity current, evidenced by wave-like activity in the instantaneous density data of Figure 6, and a positive vertical density flux $\overline{\rho'w'}$ at the gravity current interface in Figure 10. Here, primes represent deviations of a variable from their time- and spanwise-averaged values. While the magnitude of this positive flux is small at the gravity current interface compared to the buoyant plume, it clearly grows as the current moves downstream, and only emerges for $\theta = 10$.

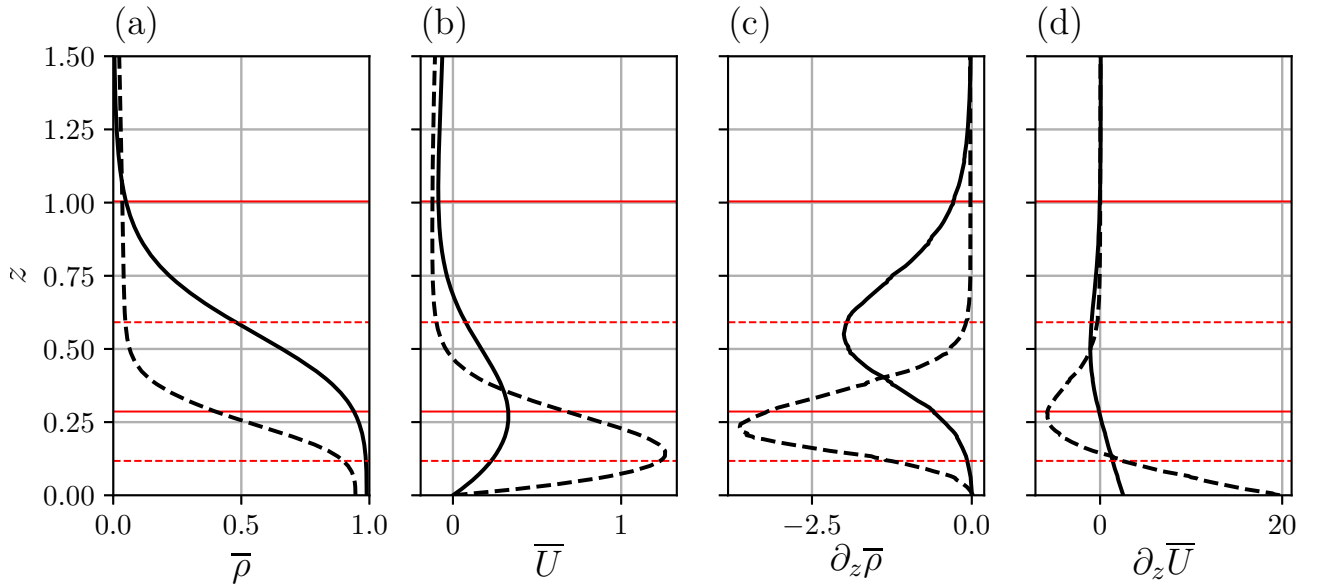


Figure 9: Temporally and spanwise-averaged density (a) and streamwise velocity (b) with respective vertical derivatives in (c) and (d) at $x = 5$. Horizontal lines approximate the bounds of the interface, quantified as the z values corresponding to 90% bounds on $\bar{\rho}$. Linestyles denote cases with $\theta = 0$ (solid lines) and $\theta = 10$ (dashed lines).

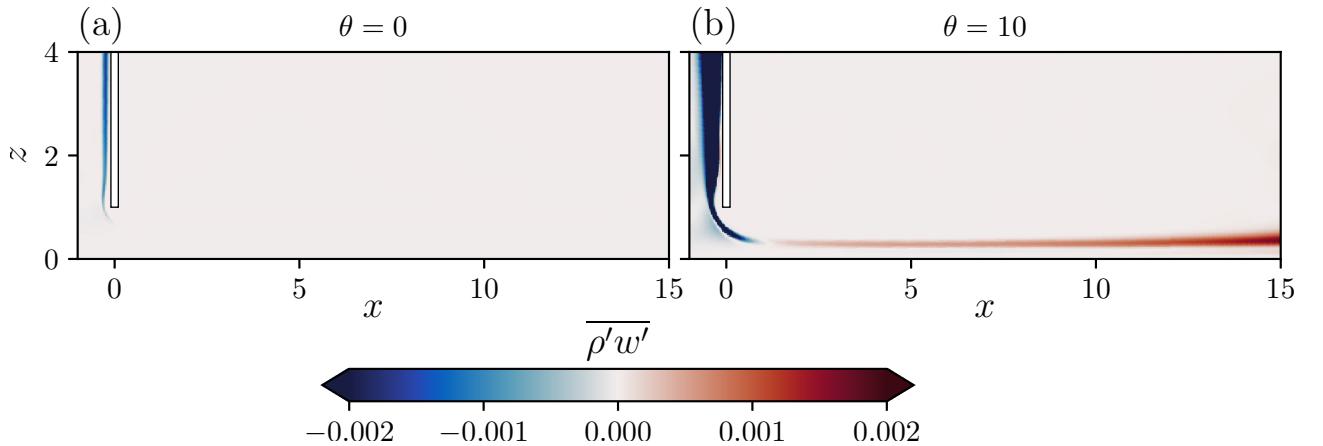


Figure 10: Temporally and spanwise-averaged vertical density flux for $\theta = 0$ (a) and $\theta = 10$ (b).

The vertical density flux at the interface between the two fluids appears to be generated by wave-like motion when observing the fluctuating vertical velocity and density fields (Figures 11 and 12). For $\theta = 0$ only weak fluctuations in density are present at the interface, yet at $\theta = 10$ we observe regions of positive and negative density fluctuations along the interface between the two fluids. In addition, we see a similar pattern in the vertical velocity field, although there appears to be some sheared structure to these contours. Fluctuations in the velocity and density field are indicative of wave-like activity at the density interface, yet the nature of these waves is unclear from these figures.

In order to quantify the spatio-temporal structure of these waves we adopt Spectral Proper-Orthogonal Decomposition (SPOD) using the method of Schmidt & Colonius (2020). Spanwise-normal slice data are organised into snapshots $\mathbf{r}(\mathbf{x}, t)$ consisting of vertical velocity and density fluctuations. Following the method of Welch, snapshots are split into 38 consecutive and temporally overlapping (with a 50% overlap) blocks ($N_{\text{blk}} = 38$), each containing 2048 snapshots. Fourier transforms are performed on each block, using a Hamming

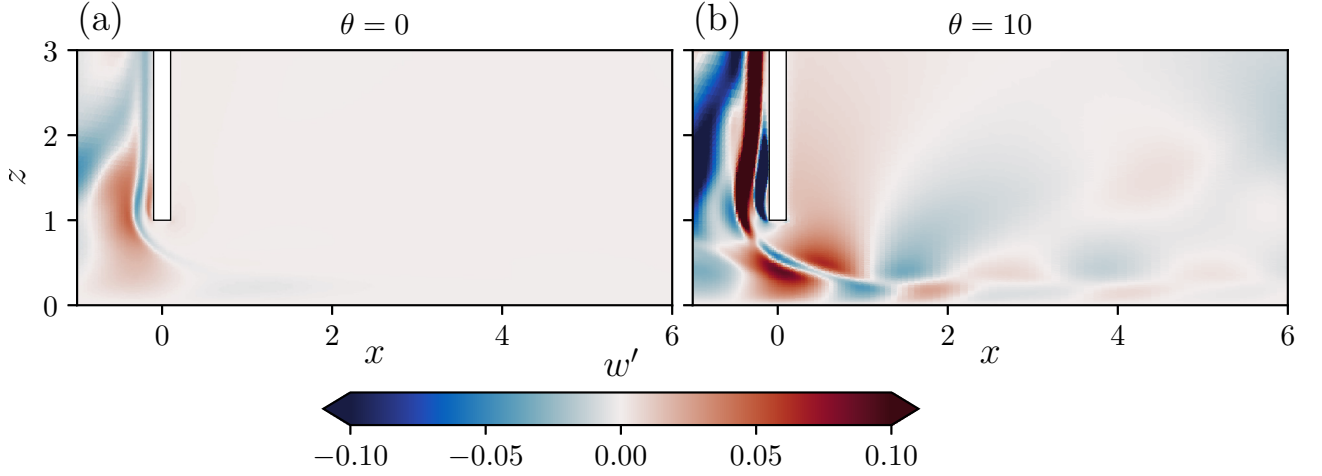


Figure 11: Fluctuating vertical velocity fields on a y normal slice at $y = \pi/2$ for $\theta = 0$ (a) and $\theta = 10$ (b).

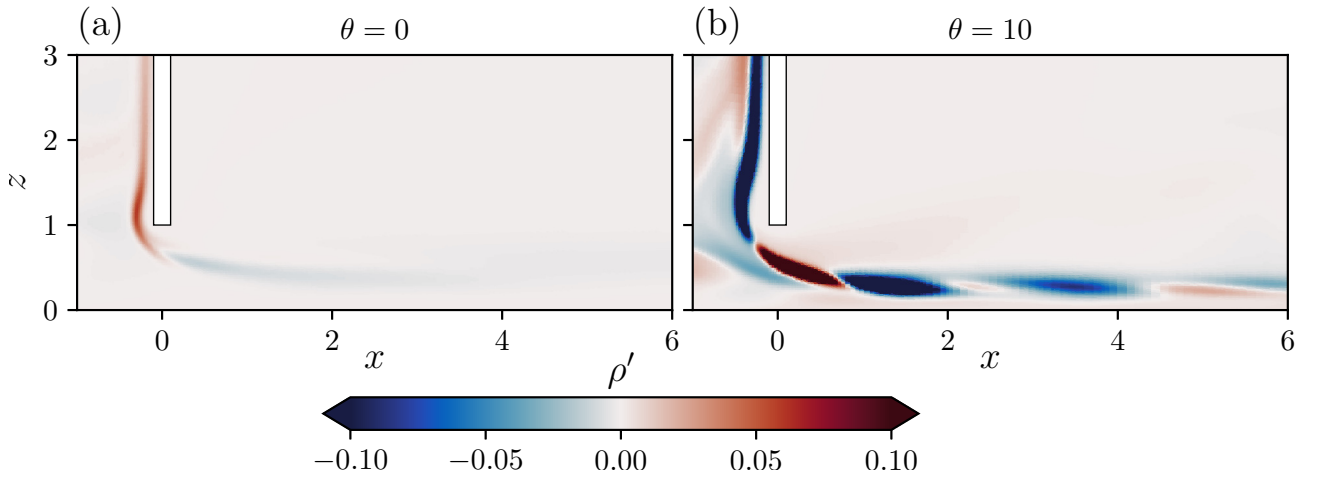


Figure 12: Fluctuating density fields on a y normal slice at $y = \pi/2$ for $\theta = 0$ (a) and $\theta = 10$ (b).

window, to obtain $\hat{\mathbf{r}}(\mathbf{x}, \omega)$. For each frequency the data $\hat{\mathbf{r}}$ are arranged into a matrix \hat{R} ,

$$\hat{R} = \begin{bmatrix} \vdots & \vdots & \dots & \vdots \\ \hat{\mathbf{r}}^1 & \hat{\mathbf{r}}^2 & \dots & \hat{\mathbf{r}}^N \\ \vdots & \vdots & \dots & \vdots \end{bmatrix}, \quad \hat{R} \in \mathbf{C}^{M \times N} \quad (21)$$

where M is the total number of degrees of freedom (the number of spatial grid points multiplied by the number of variables: vertical velocity and density fluctuations) and N is the number of realisations (equal to the number of data blocks, N_{blk}) at the given frequency. The SPOD modes, $\hat{\Phi}$, are eigenvectors of the sample cross-spectral density \hat{C} , given by

$$\hat{C} = \frac{1}{N-1} \hat{R} \hat{R}^H. \quad (22)$$

Eigenvectors $\hat{\Phi}$ have corresponding eigenvalues $\hat{\Lambda}$ which quantify the energy content of a given mode. For more information, see Schmidt & Colonius (2020).

The SPOD of y -normal slice data is shown in Figure 13. Modal energies are presented in panel (a) which shows a clear and distinct peak at $\omega = 1.72$. Here, there is an order of magnitude difference between energies associated to the first and second modes, shown in panel (b). The second and third peaks in modal energy occur at higher frequencies with lower magnitudes and occur with frequencies at scalar multiples of the frequency associated with the largest peak, indicative of non-linear mode-mode interactions. The structure of the marked mode in panel (a) is shown in panels (c) and (d), respectively presenting the vertical velocity and density components. We see a very clear spatio-temporal structure with a dominant streamwise wavenumber.

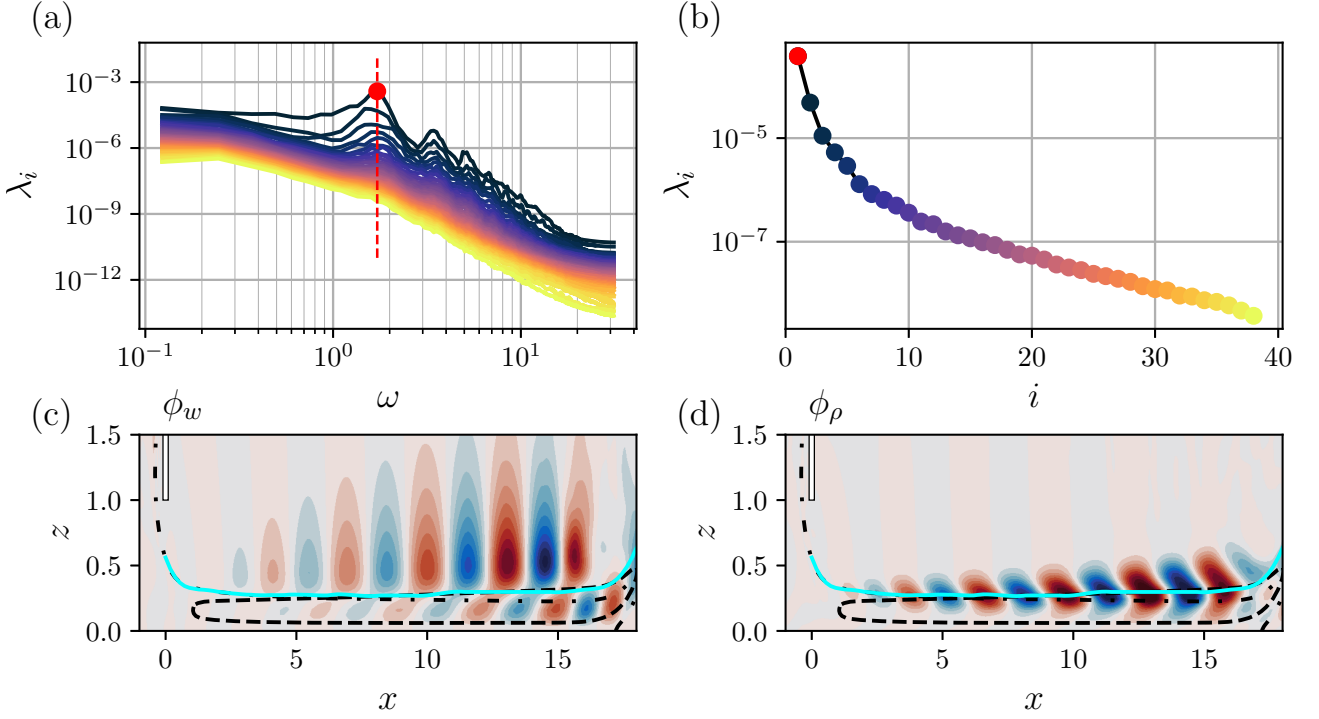


Figure 13: Spectral-POD of y -normal slice data for $\theta = 10$. (a) shows eigenvalues λ_i as a function of temporal frequency, ω , where the index i represents the mode number of $\hat{\Lambda}$, ordered by their magnitude. (b) shows eigenvalues for the frequency marked with the dashed line in (a) corresponding to the maximum energy in the decomposition. The spatial structure of the mode marked in (a) is reported in panels (c) and (d), with the vertical velocity component in (c) and density in (d). The dashed lines in (c) and (d) represent critical levels where the modal wavespeed is equal to the mean streamwise velocity, $c = \omega/k_x = \bar{U}$, where k_x is obtained from a Fourier transform of ϕ_ρ (with windowing in x) in panel (d). The dash-dotted lines in (c) and (d) represent the density interface at $\bar{\rho} = 0.5$. The solid lines in (c) and (d) represent the z position of the maximum (negative) shear at a given x position (see Figure 9).

The magnitude of the mode and its spatial extent in z grows as it moves downstream. The locus of the mid-density isopycnals (η) where $\rho = 0.5$ are marked by the dashed-dotted line in panels (c) and (d). The $\rho = 0.5$ isopycnals yield an approximate location of the density interface which also coincides with the velocity interface where the shear is maximum owing to $Pr = 1$ chosen for this study (see Figure 9). Therefore the dashed-dotted lines also mark the location of the pycnocline. There is a clear influence of shear on the modes which creates vertical distortion in the distribution of the modes.

We find that shearing of the mode occurs directly in the location of maximum (negative) shear, marked with the solid lines in Figure 13 (note that the maximum positive shear occurs at the wall where $\rho \approx \rho_1$). For much of x , the location of maximum negative shear coincides with the location where we see critical levels, where the modal phase speed $c = \omega/k_x$ matches the background streamwise velocity, \bar{U} . Here the wavenumber k_x has been obtained by taking a Fourier transform of the density contours in panel (d) and averaging in the vertical direction. The subsequent spectral energy has a single and distinct peak at $k_x = 1.88$ (not shown for brevity). This dominant wavenumber suggests a streamwise length scale of $\lambda_x = 3.44$ which from inspection is consistent with the distance between peaks of the streamwise varying modes in Figure 13 (c,d). This analysis shows that the dominant mode has a well defined and distinct frequency and streamwise wavenumber, and therefore phasespeed, with no spatial dependence. Critical levels occur at the region of strongest (negative) shear where we observe distortion of the modes. For comparison, we have also reported the density interface in Figure 13, but note that the centre of the modes correlates better with the critical levels and (negative) shear maximum, except at small x where the differences between the two lines are nearly indistinguishable.

There are several key features of the dominant SPOD mode that indicate the mean flow is susceptible to instability at the interface, and that the dominant SPOD mode is a spatially and temporally developing interfacial instability. Firstly, note the comparable steepness in the mean velocity and density profiles at the density interface (Figure 9), and their large respective gradients, particularly for $\theta = 10$. From inspection of the profiles in Figure 9 we see that the gradient Richardson number $Ri_g = -\partial_z \bar{\rho} / (\partial_z \bar{U})^2$ is less than the critical value

of 0.25 at the region of strongest shear for $\theta = 10$, indicating the flow may be susceptible to shear instability. However, we caution a deeper interpretation of this result given that the flow is spatially developing, has shear and density profiles strongly spatially dependent, and has the density interface occur reasonably close to the lower boundary. Secondly, note that the density mode extrema coincide with the regions of maximum (negative) shear, and critical levels. Instabilities in stratified shear layers grow, and are dependent, on inflection points in shear (Smyth & Carpenter, 2019). The coincidence of critical levels at the location of maximum (negative) shear indicates a transfer of energy from the instability to the mean flow, which is also reflected by the increase in vertical density flux $\overline{\rho'w'}$ as the instability is advected downstream (Figure 12). The peaks in vertical velocity modes ϕ_w on either side of the pycnocline as well as the existence of critical levels and the dominant short wavenumber ($k_x = 1.88$) strongly suggests that the growth in the modal energy is due to interaction of two asymmetric vorticity waves proportional to ϕ_w on either side of critical level similar to the spatially evolving Kelvin-Helmholtz instability. The peak in temporal frequency subsequently arises as a result of Doppler shift, where the instability is advected downstream by the current. However, the true nature of such instabilities requires further investigation. Additionally, the robustness of the dominant frequency and wavenumber to the choice of (Re, θ) , and computational domain size in our current SPOD analysis will be studied in future work.

5 Conclusion

In conclusion, we have approached the problem of a gravity current generated through an exchange flow under a lock gate through two approaches. First, we have constructed a shallow water model to describe locally the flow under a gate for two-layer flow down an inclined bed in which the far-field is a balance between drag and gravity. A novel method for finding fully controlled solutions to the shallow water equations is presented, where a new solution method was presented that allowed for the presence of drag terms in the system.

Second, full nonlinear simulations of the Navier-Stokes equations have been conducted, with the inclusion of a so-called mask function to provide a forced buoyancy gradient to manifest long-time quasi-steady states. Spectral-POD analysis of span- and time-averaged data demonstrates the occurrence of unstable waves propagating along the density interface. These waves arise due to the susceptibility of the mean flow profiles to instability and are spatially focused at the region of maximum (negative) shear. The coincidence of critical levels with the maximum (negative) shear leads to the energy transfer from the instability to the mean flow, demonstrated by an enhanced vertical density flux as the instability is advected downstream by the current.

In future work, it will be interesting to explore if the flow parameters (speed, height etc.) of the generated gravity current can be accurately predicted via the shallow water theory over a range of initial conditions (density difference, gate height, etc.). Full three-dimensional Navier-Stokes simulations are computationally expensive, especially when exploring late-time pseudo-steady states of the system. Meanwhile, the shallow water theory is analytically tractable, and while the solution mechanism described in Section 3 requires numerical computation, these are performed in the order of seconds. The shallow water theory makes restrictive assumptions about the nature of the flow, and hence as a first step its validity must be tested against full nonlinear simulations. If reasonable agreement is found, the shallow water theory allows for exploration of gravity current generation in a larger range of parameter space. Note, however, that the question of stability must be explored via the full three-dimensional Navier-Stokes simulations. Furthermore, the modified shallow water theory presented here is applicable to other applications, such as gravity current interaction with bathymetry.

Once the instability has been understood through the full simulations, we will aim to capture the dynamics seen through the shallow water model. It is possible that the waves also arise in the model due to the steady state solution ceasing to exist at steep angles, and thus the only solution would be a time dependent solution. In this case there is the possibility of a direct comparison between the waves established in the full simulations and those present in the shallow water model, which will likely be different, and the exploration of an improved model. Alternatively, it may be that the steady solution exists for arbitrarily steep slopes, in which case it may be possible to relate the onset of instability to some properties of the model. For example, an analogue of the bulk Richardson number can be constructed from the velocity and density differences between the two layers, and the vertical distance between the centres of the two layers. It may be possible to relate the onset of instability to this or another dimensionless parameter constructed purely from properties of the model.

Acknowledgements

E.W.G.S. and A.D. were supported by the EPSRC National Fellowship in Fluid Dynamics (EP/X028577/1 and EP/X028607/1 respectively). C.J.L. was supported by an Early Career Fellowship funded by the Leverhulme Trust. A.A. was supported by the European Research Council (ERC) under the European Union’s Horizon 2020 research and innovation grant no. 742480, ‘Stratified turbulence and mixing processes’ (STAMP).

References

- ARMI, L. 1986 The hydraulics of two flowing layers with different densities. *Journal of Fluid Mechanics* **163**, 27 – 58.
- ARMI, L. & FARMER, D. M. 1986 Maximal two-layer exchange through a contraction with barotropic net flow. *Journal of Fluid Mechanics* **164** (164), 27 – 51.
- BAINES, P. G. & WHITEHEAD, J. A. 2003 On multiple states in single-layer flows. *Physics of Fluids* **15**, 298–307.
- CHATTERJEE, TANMOY & PEET, YULIA T 2018 Regularization modelling for large-eddy simulation in wall-bounded turbulence: An explicit filtering-based approach. *International Journal for Numerical Methods in Fluids* **88** (1), 1–17.
- DALZIEL, S. B. 1991 Two-layer hydraulics : a functional approach. *Journal of Fluid Mechanics* **223**, 135–163.
- DALZIEL, S. B. & LANE-SERFF, G. F. 1991 The hydraulics of doorway exchange flows. *Building and Environment* **26** (2), 121–135.
- FARMER, D. M. & ARMI, L. 1986 Maximal two-layer exchange over a sill and through the combination of a sill and contraction with barotropic flow. *Journal of Fluid Mechanics* **164**, 53 – 76.
- FISCHER, PAUL, MULLEN, JULIA & OTHERS 2001 Filter-based stabilization of spectral element methods. *Comptes Rendus de l’Academie des Sciences Series I Mathematics* **332** (3), 265–270.
- GONZALEZ-JUEZ, E, MEIBURG, E & CONSTANTINESCU, G 2009 Gravity currents impinging on bottom-mounted square cylinders: flow fields and associated forces. *Journal of Fluid Mechanics* **631**, 65–102.
- HÄRTEL, CARLOS, MEIBURG, ECKART & NECKER, FRIEDER 2000 Analysis and direct numerical simulation of the flow at a gravity-current head. Part 1. Flow topology and front speed for slip and no-slip boundaries. *Journal of Fluid Mechanics* **418**, 189–212.
- HOULT, D. P. 1972 Oil spreading on the sea. *Annual Review of Fluid Mechanics* **4**, 341–368.
- JIN, CHUANG, COCO, GIOVANNI, TINOCO, RAFAEL O, RANJAN, PALLAV, SAN JUAN, JORGE, DUTTA, SOM, FRIEDRICH, HEIDE & GONG, ZHENG 2021 Large eddy simulation of three-dimensional flow structures over wave-generated ripples. *Earth Surface Processes and Landforms* .
- LAANEARU, J. & CUTHBERTSON, A. 2023 Hydraulics of stratified sill flows within varying channel geometries: investigating energy loss and mixing of maximal two-layer exchange. *Environmental Fluid Mechanics* **23**, 429–464.
- LAANEARU, J. & DAVIES, P. A. 2007 Hydraulic control of two-layer flow in “quadratic”-type channels. *Journal of Hydraulic Research* **45** (1), 3–12.
- LAI, JONATHAN K, MERZARI, ELIA & HASSAN, YASSIN A 2019 Sensitivity analyses in a buoyancy-driven closed system with high resolution CFD using boussinesq approximation and variable density models. *International Journal of Heat and Fluid Flow* **75**, 1–13.
- LANE-SERFF, G. F., BEAL, L. M. & HADFIELD, T. D. 1995 Gravity current flow over obstacles. *Journal of Fluid Mechanics* **292**, 39 – 53.
- LLOYD, CJ, DORRELL, RM & CAULFIELD, CP 2022 The coupled dynamics of internal waves and hairpin vortices in stratified plane Poiseuille flow. *Journal of Fluid Mechanics* **934**, A10.

- NABI, S. & FLYNN, M.R. 2013 The hydraulics of exchange flow between adjacent confined building zones. *Building and Environment* **59**, 76–90.
- NASR-AZADANI, MM & MEIBURG, E 2014 Turbidity currents interacting with three-dimensional seafloor topography. *Journal of Fluid Mechanics* **745**, 409–443.
- NEGRETTI, M. E., FLÒR, J.-B. & HOPFINGER, E. J. 2017 Development of gravity currents on rapidly changing slopes. *Journal of Fluid Mechanics* **833**, 70 – 97.
- NEK5000 2019 Version 19.0. *Argonne National Laboratory, Illinois* .
- OOI, SENG KEAT, CONSTANTINESCU, GEORGE & WEBER, LARRY 2009 Numerical simulations of lock-exchange compositional gravity current. *Journal of Fluid Mechanics* **635**, 361–388.
- PARI, S. A. A., KASHEFIPOUR, S. M. & GHOMESHI, M. 2017 An experimental study to determine the obstacle height required for the control of subcritical and supercritical gravity currents. *European Journal of Environmental and Civil Engineering* **21** (9), 1080–1092.
- ROTTMAN, J. W., SIMPSON, J. E. & HUNT, J. C. R. 1985 Unsteady gravity current flows over obstacles: Some observations and analysis related to the phase II trials. *Journal of Hazardous Materials* **11** (1-4), 325–340.
- SCHMIDT, OLIVER T & COLONIUS, TIM 2020 Guide to spectral proper orthogonal decomposition. *AIAA Journal* **58** (3), 1023–1033.
- SIMPSON, J. E. 1982 Gravity currents in the laboratory, atmosphere, and ocean. *Annual Review of Fluid Mechanics* **14**, 213–234.
- SIMPSON, J. E. 1997 Gravity Currents in the Environment and the Laboratory, 2nd edn. Cambridge University Press.
- SMYTH, WILLIAM D & CARPENTER, JEFFREY R 2019 Instability in geophysical flows. Cambridge University Press.
- TOKYAY, TALIA & CONSTANTINESCU, GEORGE 2015 The effects of a submerged non-erodible triangular obstacle on bottom propagating gravity currents. *Physics of fluids* **27** (5).
- UNGARISH, M. 2020 Gravity Currents and Intrusions, Analysis and Prediction. Environmental Fluid Mechanics 1. World Scientific.
- WU, CHING-SEN & OUYANG, HUEI-TAU 2020 Flow morphology in bottom-propagating gravity currents over immersed obstacles. *AIP Advances* **10** (11).
- ZHU, D. Z. & LAWRENCE, G. A. 2000 Hydraulics of exchange flows. *Journal of Hydraulic Engineering* **126** (12), 921–928.
- ZHU, LU, ATOUFI, AMIR, LEFAUVE, ADRIEN, TAYLOR, JOHN R., KERSWELL, RICH R., DALZIEL, STUART B., LAWRENCE, GREGORY A. & LINDEN, P.F. 2023 Stratified inclined duct: direct numerical simulations. *Journal of Fluid Mechanics* **969**, A20.